Role of cobalt in Co-ZnO nanoflower gas sensors for the detection of low concentration of VOCs

Yifan Luo[1, 2, 3], Ahmadou Ly[4], Driss Lahem[4], Justin D.M. Martin[5], Anne-Claude Romain[5], Chao Zhang[1,], Marc Debliquy[3,*]*

1. College of Mechanical Engineering, Yangzhou University, Yangzhou 225127, PR China
2. College of Chemistry and Chemical Engineering, Yangzhou University, Yangzhou 225002, PR China
3. Service de Science des Matériaux, Faculté Polytechnique, University of Mons, Mons 7000, Belgium
4. Material Science Department, Materia Nova ASBL, Mons 7000, Belgium
5. University of Liege, Arlon Campus Environment, Sensing of Atmospheres and Monitoring, UR Spheres; Belgium.

* Corresponding authors
Prof. Chao Zhang
College of Mechanical Engineering
Yangzhou University
Huayang West Road 196
Yangzhou 225127, Jiangsu Province
P.R. China

Tel/Fax: +86-514-87436008
Email: zhangc@yzu.edu.cn
zhangchao_cqu@hotmail.com

Prof. Marc Debliquy
Science de Matériaux

University of Mons
Rue de l'Epargne 56,
7000 Mons,
Belgium

Tel: +32-65374415
E-mail: Marc.DEBLIQUY@umons.ac.be

Abstract As a non-invasive detection method, breath analysis for the diagnosis of lung cancer has been a hotspot in the medical field. Using an electronic nose to achieve the breath analysis is a popular choice. Herein, cobalt-ZnO sensors which have high response to low concentration volatile organic compounds were fabricated as sensors in electronic noses for the diagnosis of lung cancer. The Co-ZnO samples were synthesized via wet chemical method and drop coated onto the alumina substrates equipped with gold interdigitated electrodes after calcination. The as-synthesized materials were characterized by SEM/EDX, XRD, FT-IR and XPS to observe their microstructure, crystal phase, and electronic state of Co atom in the samples. The sensors were tested with various VOCs at different temperatures using artificial breath. At the same time, the stability of the sensor was tested. The sensor showed different optimal temperatures and target gas with different amounts of Co^{2+} addition. The improvement in the sensing performance could be explained by the different phases of Co in the sensing layers.

Keywords: ZnO; Co doping; p-n heterojunctions; gas sensor; VOCs; lung cancer

1. Introduction

In modern medical fields, developing non-invasive diagnosis methods for critical illnesses, such as diabetes or cancers, has become a hotspot for researchers. Breath analysis is an efficient method for the diagnosis of different kinds of diseases such as diabetes, asthma and cancers by detecting the concentration change of some gases in exhaled breath, which are considered as biomarkers [1-5]. Most lung cancer biomarkers in exhaled breath are volatile organic compounds (VOCs) such as isopropanol, acetone, isoprene [6-8], etc. Usually, breath analysis is done by gas chromatography coupled with mass spectrometry (GC-MS) [9, 10]. Although it is accurate and suitable for detecting gases at low concentrations, this method requires cumbersome, expensive equipment and skilled technicians which causes a lot of trouble for the widely use of this method. As a result, it is necessary to develop a small and user friendly device which can be easily used in doctors' offices. The electronic nose (e-nose) is one of the

choices [11-14]. The working mechanism of an e-nose is similar to human's nose. Typically, an e-nose consists of four parts: delivery system, sensor array, signal processing and pattern recognition. The sample delivery system enables the generation of the headspace of a sample, which is the fraction analyzed. The system then injects this headspace into the detection system of the electronic nose. The sample delivery system is essential to guarantee stable operating conditions. The detection system, which consists of a sensor array, is the part for the reaction. When in contact with target gases, the sensors react, giving a signal (usually electrical signal). After that, the electronic system combines the signals coming from different sensors and the recognition pattern allows to discriminate odors. Generally, the sensors in the e-nose are sensitive to all kinds of gases with limited selectivity. However, for breath analysis, especially those for lung cancers, since most of the concentrations of the biomarkers are low (ppb level), the sensors need to be sensitive to the target gases. As a result, to fabricate a good e-nose for breath analysis, developing sensitive sensors for sub-ppm concentrations is an essential point.

Semiconductor gas sensors, especially those using semiconducting metal oxides (MOX), such as zinc oxide (ZnO), are good candidates for the sensors in e-nose systems. Typically, MOX sensors have a relatively high response, low cost and are easy to fabricate [15-17]. Some studies about using sensors based on ZnO to detect low concentration VOCs have been done in the past decade. For example, Zhu et al. [18] synthesized coral rock like ZnO by hydrothermal method for the detection of VOCs. Their sensor had a high response to 600 ppm of several kinds of VOCs at a high working temperature. Li et al. [19] prepared MOF derived ZnO nanocage to detect acetone, having good responses to ppb level of VOCs at 300 $^{\circ}$C. Meng et al. [20] introduced flower-like structures with porous single-crystalline ZnO nanosheets for ethanol sensing. This sensor worked at around 225 $^{\circ}$C but had a poor response.

According to those references, the problem of pure ZnO sensors is the inadequate response to the target VOC gas when the concentration is low. For breath analysis, generally, the concentrations of the biomarkers are down to the ppb range, so the responses of those MOX sensors are not good enough. At the same time, ZnO is not

selective for the different kinds of VOCs. To build an e-nose, sensors with different responses need to be combined. As a result, it is essential to modify the MOX sensors to modify their gas sensing performances. There are several possible methods, such as doping, building heterojunctions and achieving morphologies with large specific surface area [21-24], which can improve the gas-sensing properties of metal oxides. For example, the creation of p-n junction using n-type (SnO_2 In_2O_3, TiO_2, WO_3, ZnO,) and p-type (Cr_2O_3, Co_3O_4, NiO, CuO, PdO, Ag_2O, CdO) semiconductor oxides has been reported to improve the sensing performance of prepared composites. [25]

In this work, we prepared Co-ZnO composites with unique morphology to increase the specific surface area of the sensing materials and to have the synergetic effect of the cobalt oxide (CoO and Co_3O_4) and ZnO. It is well known that both CoO and Co_3O_4 have a narrowed bandgap compared with ZnO, which means that the two materials can form a p-n heterojunction between ZnO and cobalt oxide, which may increase the response and change the selectivity of the sensors. Meanwhile, when the amount of Co is low, the doping effect of Co can tune the bandgap of ZnO and improve its sensing performance. Besides, it is well known that cobalt oxide is catalytically active in low temperature oxidation of some reducing gases [26]. As a result, the Co-ZnO sensors show good responses to low concentrations of isopropanol and acetone, which are considered as biomarkers of lung cancer.

2 Materials and methods

2.1 Materials

All the chemicals mentioned in this paper were ordered from VWR Belgium and without any further purification.

2.2 Synthesis of the Co_3O_4-ZnO composites

The Co_3O_4-ZnO composites were synthesized via a chemical precipitation method. First, x mmol $Co(NO_3)_2$•$6H_2O$ and 3-x mmol $Zn(NO_3)_2$•$6H_2O$ were dissolved in 55 ml of deionized (DI) water, which was marked as solution A. To make different contents of Co and Zn, the x here were set as 0.3, 0.6, 0.9, 1.2 and 1.5 (10 at%, 20 at%, 30 at%, 40 at% and 50 at% Co, respectively). At the same time, 30 mmol of 2-Methylimidazole

(MeIM) was dissolved in 50 mmol of DI water and magnetically stirred until the solution became clear. The solution was marked as solution B. After all the solutions were well mixed, solution B was poured into solution A, then 15.5 ml of 29% ammonia was added into the solution immediately. Afterward, the purple solution was magnetically stirred at room temperature for 2 h. The purple precipitates were centrifugated and washed with DI water and ethanol several times and then dried at 80 ^{o}C overnight in an oven. The synthesis steps are shown in Figure 1. To prepare the Co_3O_4-ZnO, the as-prepared purple powders were calcinated at 500 ^{o}C for 2 h, and the heating rate was set as 5 ^{o}C/min. The obtained samples are named as 10Co, 20Co 30Co 40Co and 50Co, respectively. For comparison, a pure Co_3O_4 was made by the same method by adding only 3 mmol of $Co(NO_3)_2$•$6H_2O$ in solution A.

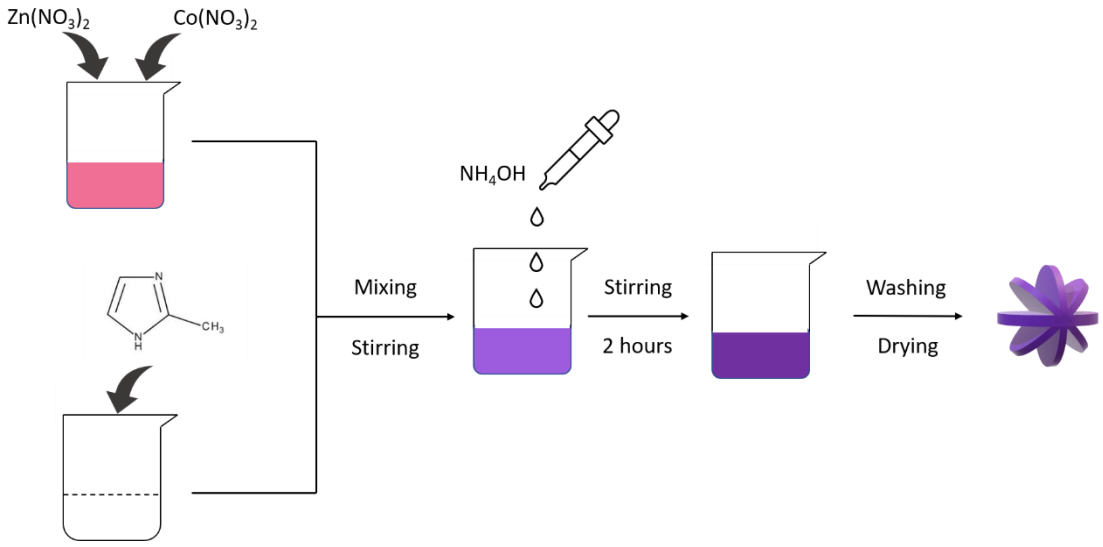

Figure 1. Synthesis method of the Co-ZnO nanoflowers.

2.3 Materials Characterization

X-ray diffraction (XRD, Panalytical Empyrean) with $CuK_{\alpha 1}$ radiation (λ = 1.5405 Å) was carried out to confirm the phase of the ZnO and Co_3O_4 and calculate the size of the grains of both phases. The scanning range of 2θ in the XRD tests was chosen from 20^{o} to 90^{o}.

A field-emission scanning electron microscopy (FE-SEM, Hitachi SU8020) was used to observe the microstructure of the as-synthesized powders. EDX mapping was

used to detect the distribution of the Co and Zn atoms in the final products. X-ray photoelectron spectroscopy (XPS, XPS Phi Versa Probe 5000) was used to analyze the state of the cobalt in the complex. The pressure in the XPS analysis chamber is in the order of 1.10^{-9} Torr. The X-ray source is monochromatized and the line used is the Al Kα line (E = 1486.7 eV). The power applied to the X-ray source is 50W. The beam voltage is 15000V. The Fourier-transform infrared spectroscopy (FT-IR) test was carried out by an IFS 66v/s FTIR spectrometer from BRUKER. The scanning range is from 3000 to 450 cm^{-1} and the operation mode of the FT-IR is in absorbance mode.

2.4 Fabrication of sensors and gas sensing test

All the layers in this experiment were deposited by drop-casting on the alumina substrates. One side of the alumina substrates is equipped with gold interdigitated electrodes. The distance between the 7 fingers is 250 μm. On the other side, a platinum coil is equipped for the heating of the sensors. To prepare the sensing layers, 50 mg of as-prepared Co_3O_4-ZnO powders were mixed with 0.5 ml of DI water and then coated on the gold electrodes by drop coating. The coating thickness was measured by an optical profilometer from Nanojura. The coating thickness is in the range of 100 to 200 μm. After that, the coating was dried at 105 ^oC in an oven overnight. Before the sensing test, the sensors were pre-heated at 350 ^oC for three days to remove the possible organics remaining in the layers and ensure a stable baseline. The gas sensing test was carried out in a homemade testing system. The testing system and the testing method are the same as introduced in our former work [27]. The gas flow was controlled by a group of flow meters (Bronkhorst). The flow to the testing chamber was always kept at 1000 sccm. The working temperature of the sensors was controlled by the Pt wire by adding a certain voltage and measuring its resistance change. For the target gases, methanol, ethanol, isopropanol and acetone were obtained by means of bubblers filled with an aqueous solution of the target gas. The vapor concentration is calculated according to Henry's law. In the experiments, a certain amount of VOCs liquid was added into 250 mL of deionized water and well mixed to make the solution in a bubbler.

The solution concentration is calculated by the following equation: $C_l = \frac{K_H \times C_g}{1000000}$. In the equation, C_l is the concentration of the VOCs solution with the unit of mol/L; K_H is Henry's constant of the VOCs with the unit of mol/kg/bar and C_g is the concentration of the generated VOCs gas with the unit of ppm. after that the solution was kept in water bath at 25 °C. To generate the gas, a certain airflow is controlled by a flowmeter and mixed with the dry and 100% RH air to generate VOCs with different concentrations. In this step, the total gas flow was kept at 1000 sccm. The concentration of the VOCs generated from the bubbler was checked by a commercial TVOC meter (Graywolf). The result of the test is listed in Table S1 and Table S2. The ammonia (NH_3) and formaldehyde (HCOH) were directly gained from the gas bottle bought from Air Liquide+Belgium. To study the effect of high concentration CO_2, a gas mixture with 5% CO_2, 16% O_2 and 79% N_2 was used as the background gas. To further simulate the human exhaled breath, a gas mixture of 79% N_2, 16% O_2, 5% CO_2, 20 ppb acetaldehyde, 100 ppb isoprene, 200 ppb ethanol, 500 ppb acetone and 500 ppb methanol was also used as the background gases instead of synthetic air. The response is defined as $S=(R_a-R_g)/R_g$ when the sensor resistance is decreasing in the target gas; when the resistance is increasing, the response is $S = (R_g-R_a)/R_a$. In the equations above, S is the sensor response, R_g is the electrical resistance of the sensor in target gas and R_a is the electrical resistance of the sensor in synthetic air. The response and recovery times of the sensors were defined as the time needed to reach 90% of the maximum response and recover to 110% of the baseline.

3. Results and discussion

3.1 Characterization of the materials

After the heat treatment, the as-synthesized purple powders turned to different colors. The ones with lower than 20 at% Co showed a dark green color while those having more than 30 at% Co were black. The difference between the color indicated that the Co might have different oxidation states.

First, to check the morphology of the as-synthesized powders, SEM was used. Figure 2(a) and (b) display the microstructure of the pure Co_3O_4 before and after

calcination. The obtained Co_3O_4 showed a nanosheet-assembled flower-like structure, as is shown in Figure 2(a). The thickness of each nanosheet was around 200 nm, while the diameter of a flower was about 4 μm. After the calcination in air, the morphology and the size of the flowers do not change a lot. The only difference is that the sheet had a slight bending. Figures 2(c) and 2(d) show the morphology of 10Co before and after calcination. Compared with the pure Co_3O_4, the 10Co sample remained the nanosheet-assembled flower structure, but after the calcination, a large number of tiny pores appeared on the surface of the nanosheets. The average size of those pores is ~36 nm. Also, according to Figures 2(e) and 2(f), the increase of Co content didn't significantly influence the structure of the materials. To check the distribution of the Zn and Co atoms, we performed EDX mapping on the 20Co sample before and after calcination. The result is shown in Figure 3, Table 1 and 2. Before calcination, Zn, Co, C, N and O can be found in the powders, as shown in Figure 3(a). After calcination (Figure 3(b)), N disappears, only a small amount of C left, which is coming from the tape used in the test more O appears at the same position with Zn and Co, which indicated that the organic parts in the powders were completely removed during the calcination step.

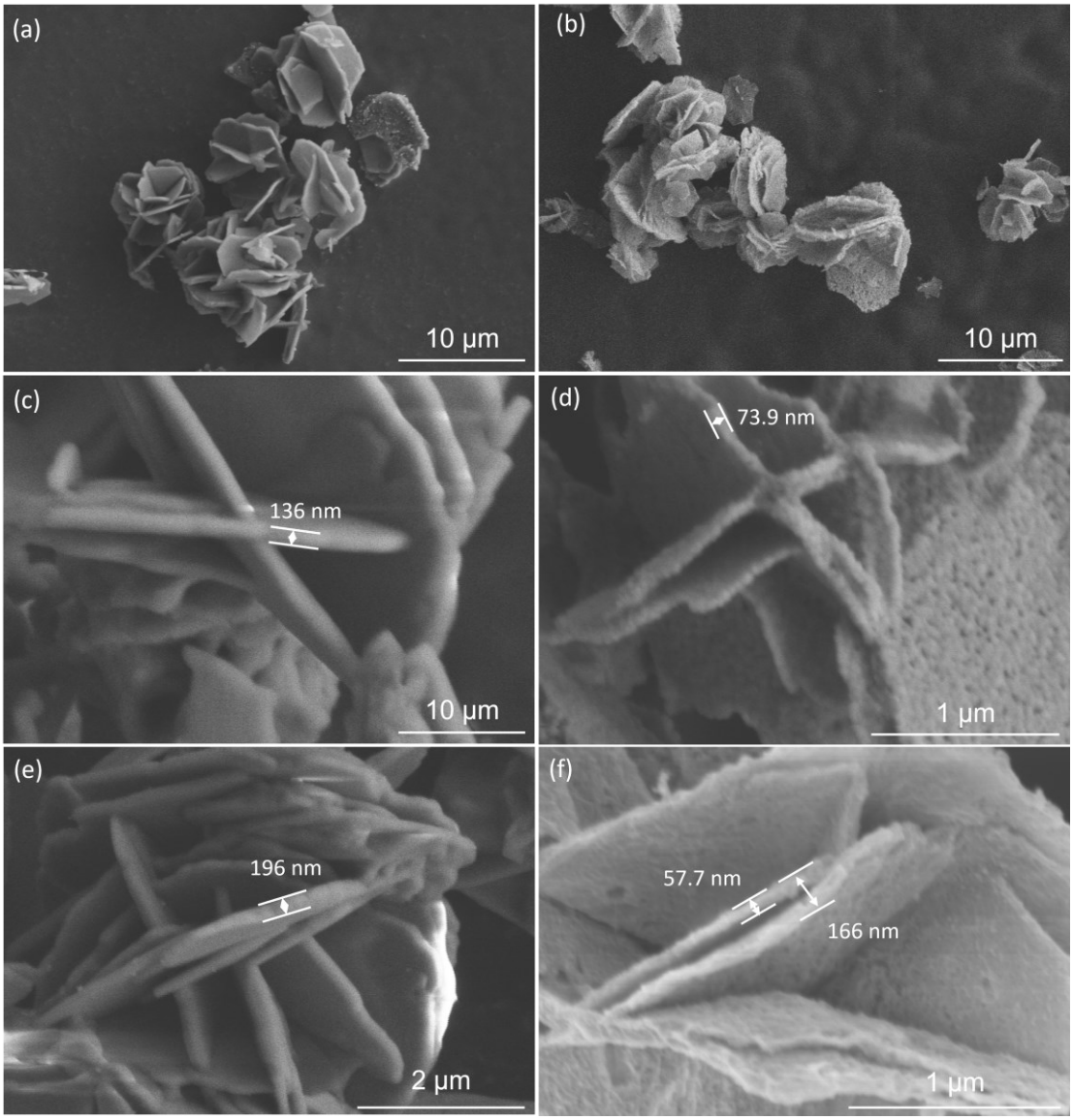

Figure 2. SEM images of (a) pure Co-imidazole before calcination (Co_3O_4) (b) after calcination (c) 10Co before calcination (d) 10Co after calcination (e) 40Co before calcination (f) 40Co after calcination

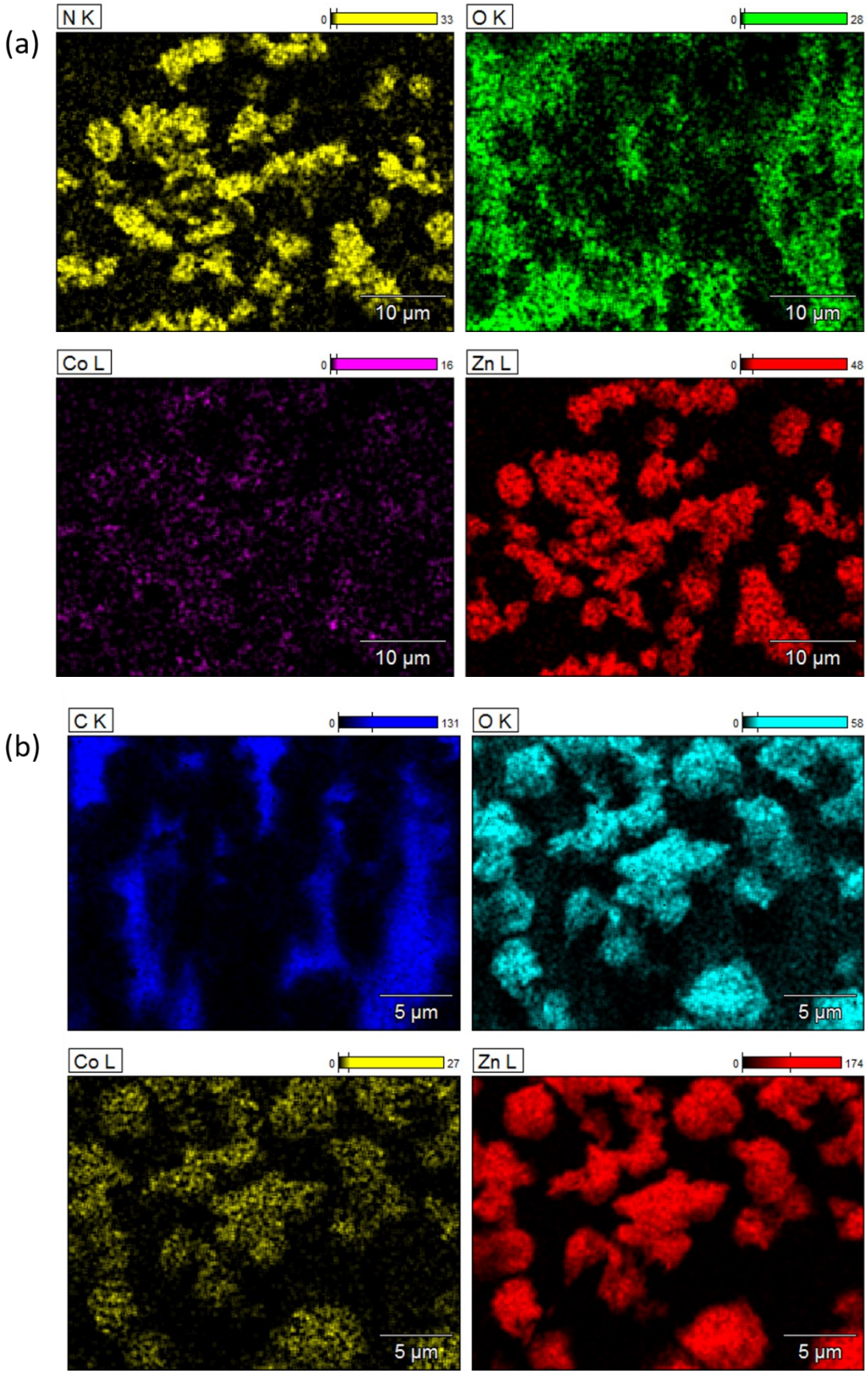

Figure 3. (a) EDX figures of N, O, Co and Zn in the 20Co powders before calcination (b) after calcination

Table 1. Element quantity of 20Co before calcination

Element Line	*Weight %*	*Weight % Error*	*Atom %*	*Atom % Error*
C K	38.6	± 0.3	50.8	± 0.8
N K	25.5	± 1.7	28.8	± 3.9
O K	15.5	± 1.1	15.4	± 2.1
Co K	2.9	± 0.2	0.8	± 0.1
Zn K	17.5	± 0.4	4.2	± 0.2
Total	100.0		100.0	

Table 2. Element quantity of 20Co after calcination

Element Line	*Weight %*	*Weight % Error*	*Atom %*	*Atom % Error*
C K	4.6	± 0.1	14.3	± 0.5
O K	17.6	± 0.2	40.9	± 1.1
Co L	9.7	± 0.5	6.1	± 0.6
Zn L	68.1	± 0.4	38.7	± 0.5
Total	100.0		100.0	

To study if the organics were well removed in the calcination step, we performed FT-IR to the 10Co, 30Co and 40Co samples. For comparison, the 10Co sample before calcination was also analyzed. Figure 4(a) exhibited the FT-IR results of the Co-ZnO samples before and after calcination. In the plot of the 10Co before calcination, peaks related to the C=N stretch bond at ~1590 cm^{-1}, the ring stretch bond at~1382 cm^{-1} and the in-plane bending of the ring at 1350-900 cm^{-1} in the MeIM can be found [28, 29], which indicated that in the flower-like structure before calcination, Zn and Co was connected by the MeIM. In all the three groups after calcination, the peaks after 750 cm^{-1} disappeared, which meant that the MeIM was eliminated during the calcinating process. At the same time, a peak at ~600 cm^{-1} appeared and was getting stronger with the increase of Co content, which is due to the formation of Co_3O_4. [30]

To study the crystal structure of those powders, we analyzed the XRD patterns of powders before and after calcination. The results are shown in Figure 4(b). Before calcination, the sample showed several strong peaks when 2θ was in the range of 10°-20°. After calcination at 500 °C, all the peaks coming from the organics disappeared. In the 10Co and 20Co samples, only peaks of hexagonal ZnO (JCPDS 36-1451) can be

found, no peaks related to CoO can be found, while in the other groups, peaks corresponding to both hexagonal ZnO and spinel cubic Co_3O_4 (JCPDS 42-1467) can be found. These facts make us think that for the 10Co and 20Co, we have a solid solution, while for higher Co content, the solubility limit has been reached and a second phase made of Co_3O_4 appears. In the 10Co and 20Co groups, the main peaks of ZnO did not have a strong shifting. Due to the similar size of Co and Zn atoms, it cannot prove that the Co was not in solid solution for the 10Co and 20Co groups. To further prove the form of Co in the composite, we used XPS to analyze the samples. Figure 5(a) was the survey of XPS. From the survey, we can only find the peaks related to C, O, Zn and Co. Figure 5(b-d) were the regions of O 1s, Zn 2p3 and Co 2p. In the O 1s region, peaks at 530.4 eV and 531.8 eV appear in all the samples, which were correlated with the lattice oxygen in ZnO and the oxygen deficiencies [31-33]. The peak at 531.8 eV was weak, proving that oxygen vacancies did not play an important role in the sensors. A peak at 529.5 eV can be found in 30Co, 40Co and 50Co. With the increase of the Co, the peak gets stronger. This peak is related to the Co^{3+} in Co_3O_4 [21], which is consistent with the result of XRD. In the Co 2p region, the $Co2p_{3/2}$ peak corresponding to Co (II) and Co (III) are located at 779.7 eV, so it is impossible to fit the peak and quantify the different oxidation states. However, it is possible to distinguish the oxidation state of Co by checking the satellite peaks. For Co^{2+}, a satellite peak appears at around 786 eV, while in Co_3O_4, the oxidation state of Co is a mixed states of Co (II) and Co (III). Generally, at 786 eV, Co (II) showed a higher intensity compared with Co_3O_4, as we can observe from Fig. 5(d). As a result, in 10Co and 20Co, Co (II) is the main part, while in 30Co, 40Co and 50Co, the Co is a mixed state of Co (II) and Co (III).According to reference [34-35] and the XRD results, we consider that there are three different kinds of Co-ZnO samples. When the atom ratio of Co is lower than 20 at%, it is considered as Co substituted ZnO, when Co is more than 40 at%, it is mostly Co_3O_4-ZnO composites. For the 30Co sample, it is more likely to be a mixed state of Co substitution and Co_3O_4-ZnO composites.

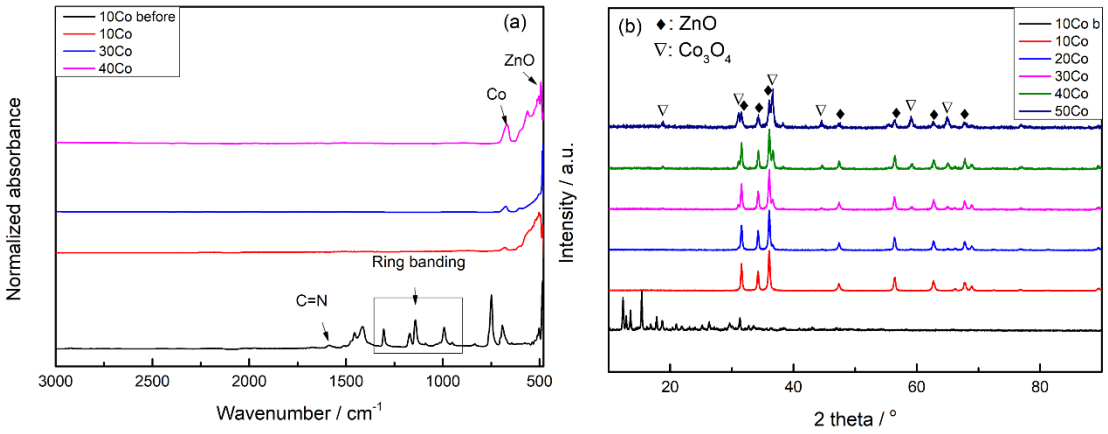

Figure 4. (a) FT-IR patterns of Co-ZnO powders with different Co contents; (b) XRD patterns of Co-ZnO powders with different Co contents.

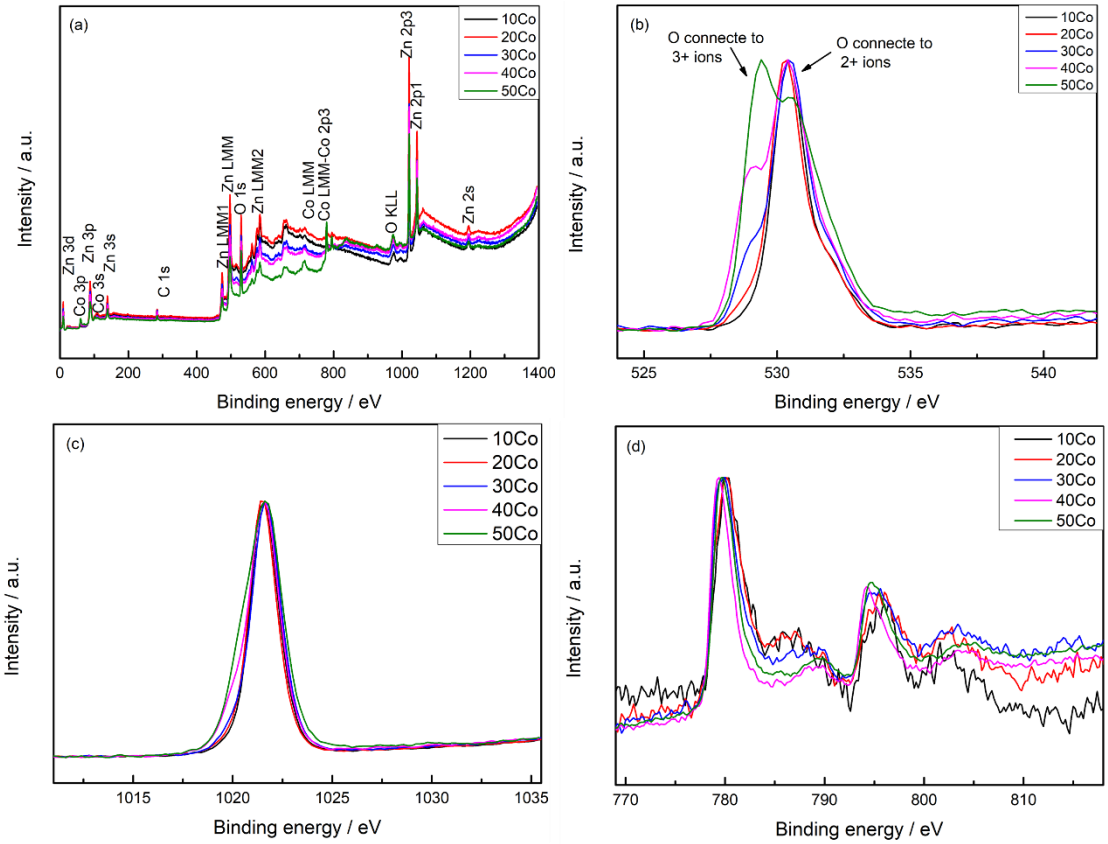

Figure 5. (a) XPS survey (b) O 1s regions (c) Zn 2p3 regions (d) Co 2p regions of 10Co to 50Co nanopowders after calcination

3.2 Gas sensing tests

To study the gas sensing performance of the Co-ZnO sensors, we first tested the

gas sensing performance to isopropanol at different operating temperatures. Several inferring gases (acetone, methanol, ethanol, formaldehyde, ammonia) were also tested.

We did it with humid air as background gas in the first step. As the sensors are designed for breath analysis, the background gas was then changed to mimic the real breath better. For this test, we use a mixture of 79% N_2, 16% O_2 and 5% CO_2 and an artificial breath as the background gas.

3.2.1. In humid air

Figure 6(a) shows the response change to 5 ppm isopropanol of different Co-ZnO sensors with an increase in operating temperature. In all the tests mentioned in this section, the relative humidity is controlled at 50%. The 10Co and 20Co reached the highest response at 225 ºC, while the 30Co and 40Co sensors had the best response at 250 ºC. For the 50Co sensor, its response to isopropanol was poor at all the temperatures we chose. Due to the high electrical resistance of the sensors and the limitation of the testing system, it is impossible to test the response at a lower operating temperature. To further study the working temperature, we tested a small temperature range around 225 ºC with a slight change of temperatures. The results can be seen in Figure 6(b). The response reaches a peak at 227 ºC, so we consider this as the optimal working temperature for this sensor. In the range of 221 to 229 ºC, the response difference between each 2 ºC is less than 20%, while the response at 225 ºC is about 10 times higher than the one at 250 ºC. So it can be concluded that around 225 ºC is the optimal working temperature range for the 10Co sensor.

Figure 6(c) shows the dynamic response of the Co-ZnO sensors to 5 ppm isopropanol. The electrical resistance decreased with the increase of Co addition. When the content of Co was higher than 30%, the resistance of the sensors decreased significantly. For the 10, 20 and 30Co sensors, their resistances at 225 ºC were in the 10^8 to 10^9 Ω range. That value for the 40Co sensor is at 10^6 Ω while the resistance of 50Co sensor was low to around 8000 Ω. This phenomenon is caused by the short circuit between the ZnO and Co_3O_4. The pure Co_3O_4 synthesized in this paper was indeed

much more conductive compared with the ZnO, whose resistance is about 200 Ω at 225 °C. When Co_3O_4 content is low, charge barriers are formed at the contact areas of the ZnO and Co_3O_4, which increases the resistance. When Co_3O_4 content kept increasing, the conductive Co_3O_4 particles contact each other and build a conductive channel in the sensing layer. The electrons are transferred through this channel, leading to the short circuit effect and significantly decreased the resistance. From this picture, another important difference exists. In the curve of 10Co, 20Co and 30Co sensors, the electrical resistance decreased when the VOCs were injected, whereas the 40Co and 50Co sensors had an increase in the resistance. So with reducing gas, the resistance of p-type semiconductor should increase and the n-type should decrease. Compared with the results in Figure 6(c), it indicates that the 10Co to 30Co sensors has an n-type semiconductor behavior, which is the same with ZnO, the 40Co and 50Co sensors showed a p-type behavior, which is close to the Co_3O_4, which is also a p-type semiconductor. This corresponds to the results of the characterizations. Co_3O_4 becomes the main phase in the 40Co and 50Co. According to the results of the characterizations, it can be concluded that the Co substituted ZnO solid solution and the Co_3O_4-ZnO composite have different sensing mechanisms. In Figure 6(d), the lnR-1/T curve of all the sensors is plotted. The curves are close to linear and the slopes become smaller with the increase of the Co amount. This can also be explained by the electrical resistance decrease due to the short circuit between the Co_3O_4 particles. According to Figure 6(e), the 10Co sensor showed the best response to 5 ppm isopropanol at 225 °C. The response and recovery times were 330 s and 475 s. In Table 3, we made a comparison between this work and some other Co-ZnO sensors for isopropanol detection. Figure 6(f) was the response change with the target gas concentration of the 10Co at 225 °C. After the fitting of the curve, the relationship between the response and concentration can be written as $S=0.00673\times C+(-4.6092 \times 10^{-7}) \times C^2$. S is the response to isopropanol at 225 °C and C represents the gas concentration with ppb unit.

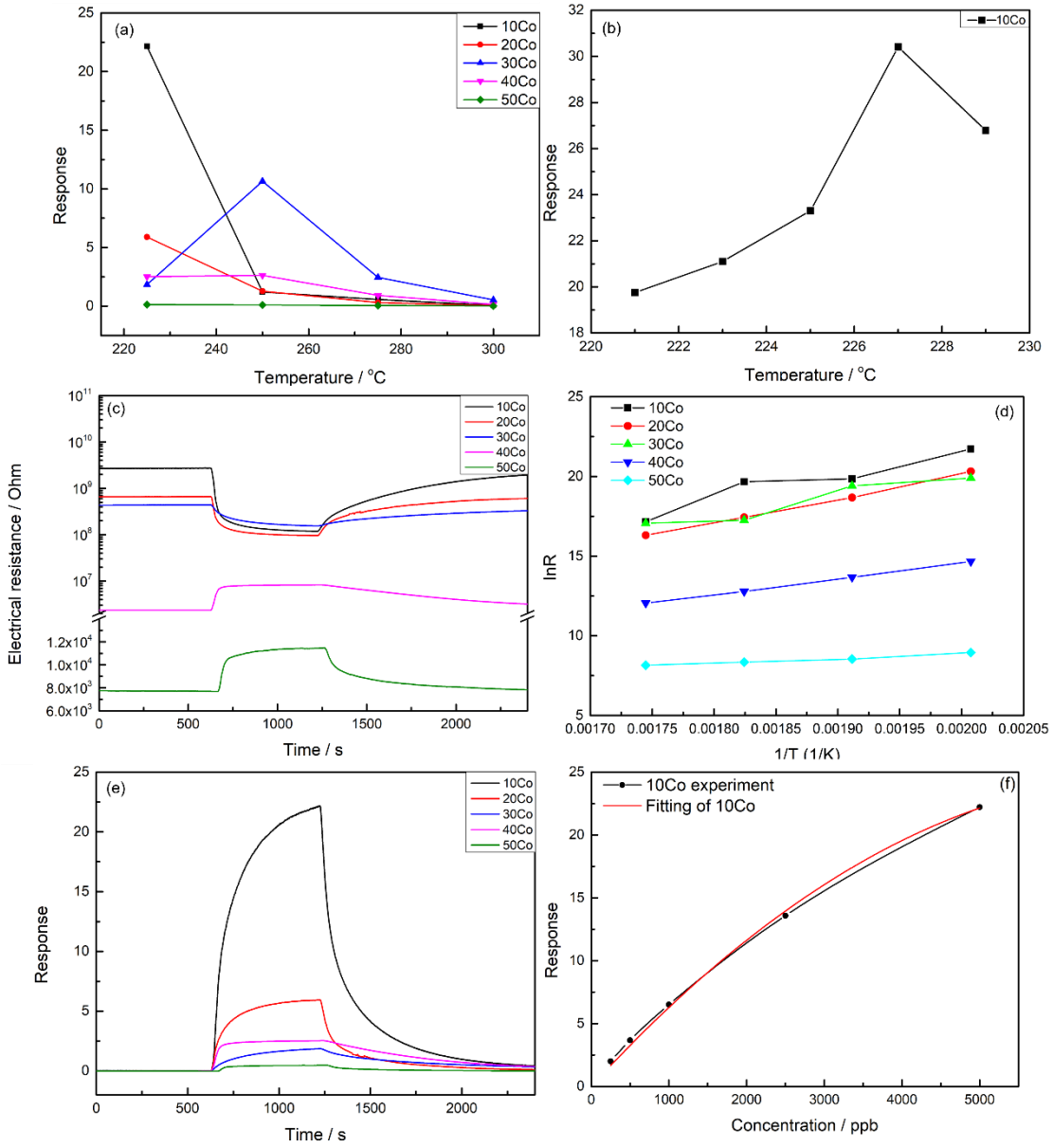

Figure 6. (a) Responses of Co-ZnO sensors to 5 ppm isopropanol at different working temperatures; (b) Response of 10Co sensor to 5 ppm isopropanol at different working temperatures close to 225 °C; (c) Electrical resistance changes of Co-ZnO sensors with 5 ppm isopropanol at 225 °C; (d) InR-1/T curves of Co-ZnO sensors in synthetic air with 50% RH; (e) Dynamic responses of the Co-ZnO sensors to 5 ppm of isopropanol at 225 °C; (f) Response of 10Co sensor with different concentrations of isopropanol at 225 °C and the mathematic fitting curve.

Table 3. Comparison of the sensing performance of different Co-ZnO related sensors for isopropanol detection

Material	Structure	Concentration	T (°C)	RH	S	Response / recovery time	Ref
ZnO	Nanotube	700 ppm	RT	Dry	47.87	3.14 min / 3.50 min	[36]
ZnO-CdO	Coral like	100 ppm	250°C	30%	17.9	16 s / 25 s	[37]
ZnO-NiO	Sheet assembled flowers	20 ppm	280°C	55%± 5%	8	-	[38]
ZnO	Nanoplate	40 ppm	125°C	Dry	6.6	190 s / 200 s	[39]
SnO_2-ZnO	Core-shell	500 ppm	300°C	-	103.3	14 s / 17 s	[40]
ZnO-ZrO_2	Coral-like	100 ppm	350°C	30%	34	19 s / 8 s	[41]
Pd@Co_3O_4-ZnO	Nanofiber	200 ppm	240°C	35%± 5%	35.5	24 s / 23 s	[42]
Co_3O_4	Nanosheet	300 ppm	100°C	30%	353	84 s / 294 s	[43]
Co_3O_4	Coral-like	1000 ppm	120°C	30%	19	29 s / 137 s	[44]
Co-ZnO	Nanoflower	5 ppm	225°C	50%	22.5	330 s/ 475 s	This work

Ethanol is a vital interference gas in the exhaled breath for lung cancer detection, so we also measured the response to ethanol under different working temperatures. Figure 7(a) indicates the response to 5 ppm ethanol under 50% RH and different working temperatures. The response to ethanol is similar to isopropanol at the optimal working temperature, but at 250 °C, 10Co and 30Co sensor showed a higher response than to isopropanol.

In addition, for the 30Co sensor, the response is different when testing acetone at a higher working temperature. As shown in Figure 7(b), when the temperature is 250 °C, this sensor showed a high response to acetone. The value can reach about 14, which is much higher compared with the other sensors. It can also be found that all the sensors which have more than 30 at% of Co work better with acetone.

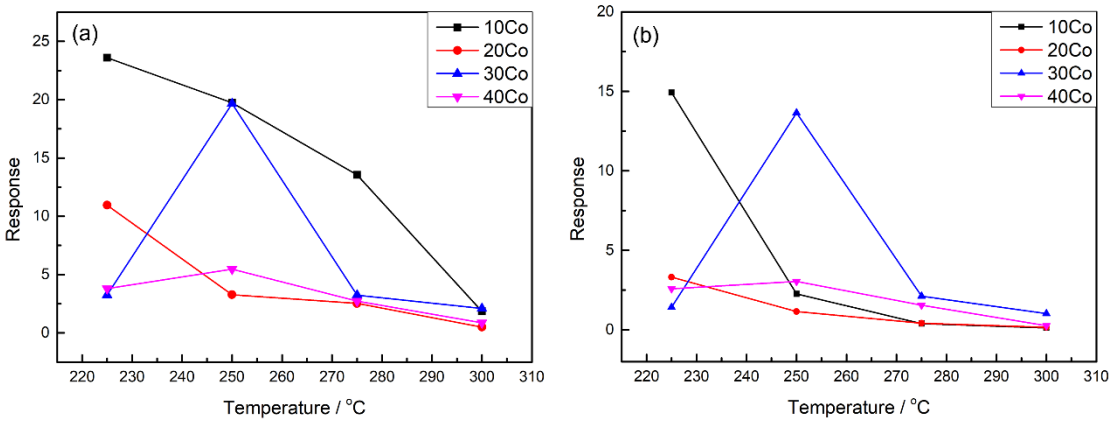

Figure 7. Responses of the Co-ZnO sensors to (a) 5 ppm ethanol (b) 5 ppm of acetone for different working temperature with 50% RH.

3.2.2. In artificial breath

Since the sensors were designed for breath analysis, we also tried to test the sensing performance with the interference of CO_2. Due to the bad performance of 50Co, in this test, it is not measured. Figure 8(a) shows the evolution of the electrical resistance (InR-1/T curve) in synthetic air and in 5% CO_2-air. As the background, the resistance in the mixture is lower for 10 to 30Co and higher for 40Co. Compared with the results we had before, this means fewer electrons were taken in the process of oxygen adsorption. It can be explained by the competitive adsorption between O_2 and CO_2. As a result, fewer target gas molecules can react with the oxygen species on the surface, which leads to a lower response, as shown in Figure 8(b). At the optimal working temperature, the response of 10Co to 5 ppm isopropanol decreases to 6.14. To further simulate the exhaled breath of human, we used an artificial breath that contains 79% N_2, 16% O_2, 5% CO_2, 20 ppb acetaldehyde, 100 ppb isoprene, 200 ppb ethanol, 500 ppb acetone and 500 ppb methanol as the background gas. All these gases are reducing and can interfere. The baseline resistance is now shifted to lower values, but the response of 10Co sensor to 500 ppb of isopropanol still can reach 1.2, while that value in air is around 4. It means that this sensor is a suitable choice for an e-nose to detect isopropanol in human exhaled breath.

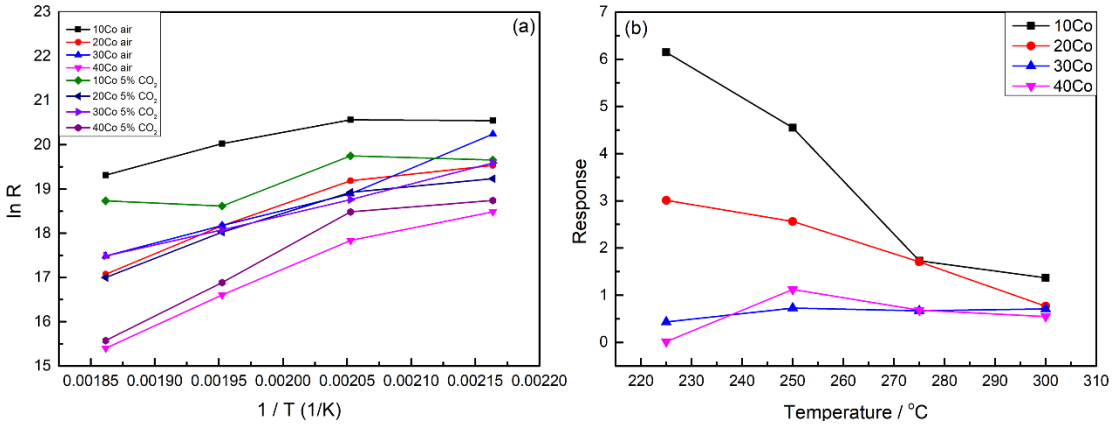

Figure 8. Evolution of (a) electrical resistance in synthetic air and in 5% CO_2-air (b) response to 5 ppm isopropanol with CO_2-air as background gas under 50% RH with operating temperature.

Other VOCs and gases are taken into consideration as well. In this paper, we chose different gases to test the response of the sensor. First, the response of 10Co sensor to different alcohols was tested. Figure 9(a) compared the responses of the 10Co sensor in different VOCs at 225 °C. The background gas was synthetic air and the relative humidity in all the tests remained at 50%. For methanol, ethanol and isopropanol, the responses to 3 gases are among 21 to 23, which means the sensor has no selectivity between the alcohol family. However, the 10Co sensor showed some selectivity between different gas families. It can distinguish between alcohol, ketones, and aldehyde when the testing conditions were the same. For NH_3, the response to even 50 ppm can be ignored because in breath, ammonia does not exceed 2 ppm. Figure 9(b) shows the response of 30Co sensors at 250 °C. Except for the working temperature, all the testing environment is the same as before. The 30Co is more sensitive to acetone compared with isopropanol. At the same time, the responses to HCOH and NH_3 remain at a relatively low level.

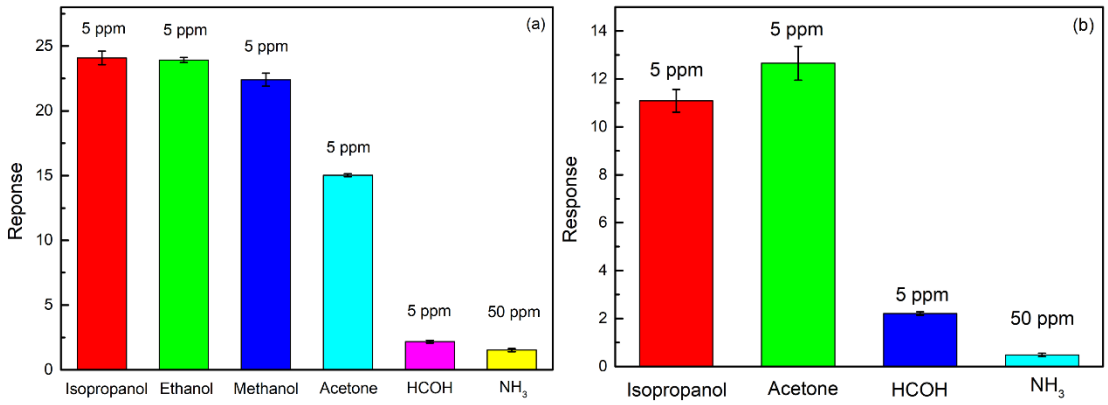

Figure 9. Selectivity of (a) 10Co sensor (c) 30Co sensor with different families of gases which are possible to appear in human's breath

Humidity is an important parameter in breath analysis due to the high relative humidity in exhaled breath. Usually, the relative humidity in exhaled breath is around 50%-90%, so we choose to test the RH effect between 50% to 90%. [45] According to Figure 10(a), the electrical resistance in air decreased a lot with the increase of relative humidity, but the resistance in isopropanol didn't change a lot, which led to the response change. The response decreased with the increase of RH. At 90% RH, the response decreased to 16.6, which is about 70% of the response value measured at 50% RH. Due to the increase of humidity, more water molecules adsorb on the surface of the sensing layer, leading to fewer reaction sites for the target gases, which is similar to the effect of CO_2.

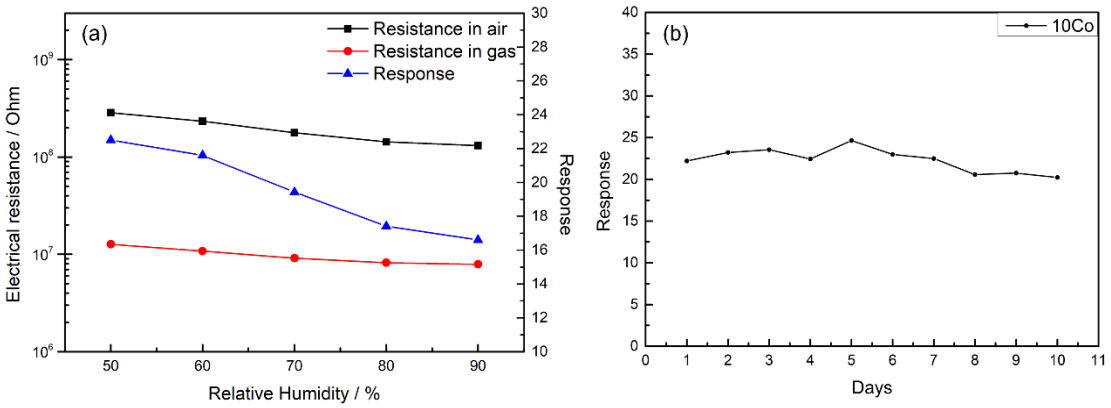

Figure 10. (a) Humidity effect to the electrical resistance and response of 10Co sensor to 5 ppm isopropanol at 225 °C; (b) Stability test of 10Co sensor with 5 ppm isopropanol at 225 °C in 10 days in air.

To study the stability of the 10Co sensor, we tested its response to 5 ppm isopropanol for 10 days at 225 °C. In all tests, the background gas was synthetic air with 50% of relative humidity. The sensor was stored in a plastic box and put under a fume hood. Before each test, the sensor was heated at working temperature until the baseline resistance was stabilized. Figure 10(b) plotted the response of the 10Co sensor in 10 days. The response values did not have any significant variation during the testing period. No obvious drift was observed. The differences were less than ±10%, which could be considered stable.

3.3 Sensing mechanism

The response or the resistance change of the sensor reflects the reaction happening on the surface of the sensing layers. First, when the sensors are exposed to air under a specific temperature, the oxygen molecules adsorb on the surface of the sensing layer, generating oxygen ions. The types of oxygen ions depend on the temperature of the sensors. In the temperature range we used in this paper, the oxygen ions should be O^- [46]. In this step, the oxygen molecules capture the free electrons in the sensing layer and increase the resistance of the sensing layer. The reaction can be written as below [47]:

$$O_2(gas) \rightarrow O_2(ads) \quad (1)$$

$$O_2(ads) + 2e^- \rightarrow 2O^- \quad (2)$$

Once the VOCs are injected into the testing chamber, the gas reacts with the adsorbed oxygen ions. The VOCs decompose to CO_2 and H_2O and release the electrons into the sensing layer, which causes the change of resistance. The general reaction can be described as below [40, 48-49]:

$$CH_3CHCH_3OH + 9O^- \rightarrow 3CO_2 + 4H_2O + 9e^- \quad (3)$$

$$CH_3COCH_3 + 8O^- \rightarrow 3CO_2 + 3H_2O + 8e^- \quad (4)$$

$$HCHO + 2O^- \rightarrow CO_2 + H_2O + 2e^- \quad (5)$$

The gas sensing process can be easily described in Figure 11(a).

According to the characterization results, there are two different existing forms of the Co in the Co-ZnO sensors. As a result, the mechanisms of improving the gas sensing performance need to be explained in two different ways. First, when the Co content is lower than 20 at%, the sensing layer is a Co substituted ZnO. In this case, the doped Co^{2+} creates some inserted energy levels in the bandgap of ZnO. According to references[50-51], the position of HOMO and LUMO of Co^{2+} is in between the valence band and conduction band of ZnO, which is shown in Figure 11(b). In this situation, the Co^{2+} dopant works as an acceptor. As a result, the electrons from the valence band of ZnO and the HOMO of Co^{2+} transfers to the LUMO of the Co^{2+} instead of the conduction band of ZnO. The energy level of the Co^{2+} LUMO is lower than the conduction band of ZnO, the energy for the excitation of the charge carriers is lower. This could be used to explain the lower operating temperature of the 10Co and 20Co sensors. Also, according to the energy difference, it can be used to explain the dark green color of the two samples. In the 40Co and 50Co sensors, the main form of Co is Co_3O_4. When in contact with the ZnO, p-n heterojunctions are built between the two oxides. According to the references [52-53], ZnO has a higher work function than Co_3O_4, so once the two materials are combined, the electrons are transferred from the conduction band of $Co_3O_4$to that of ZnO to balance the Fermi level. In this step, the electron-hole pairs are separated and, the electrons accumulate at the p-type side while the holes accumulated at the n-type side, which would generate depletion layers close to the junction areas. The depletion layers prevent the recombination of the electrons and holes, which increases the number of free charge carriers and increases the electrical resistance of the sensing layer, as shown in Figure 11(c). With more free charge carriers, more gas molecules can adsorb on the sensor surface, which leads to a high response. However, when the Co amount is too high, especially in the 50Co, Co_3O_4 becomes the main phase of the sensing material, which can be proved by the n to p-type change of the sensing behavior. Due to the extremely low resistance of the pure Co_3O_4 synthesized by this method, the Co_3O_4 particles build a conductive channel, which leads to the quick recombination of the charge carriers. With fewer charge carriers, fewer gas molecules can be adsorbed on the surface and cause a decrease in

the sensing performance. In 30Co sensor, the Co state is a mixture of both, so both mechanisms mentioned before can affect the sensing performance of the sensor, which leads to the relatively high response, high working temperature and the difference in the target gas.

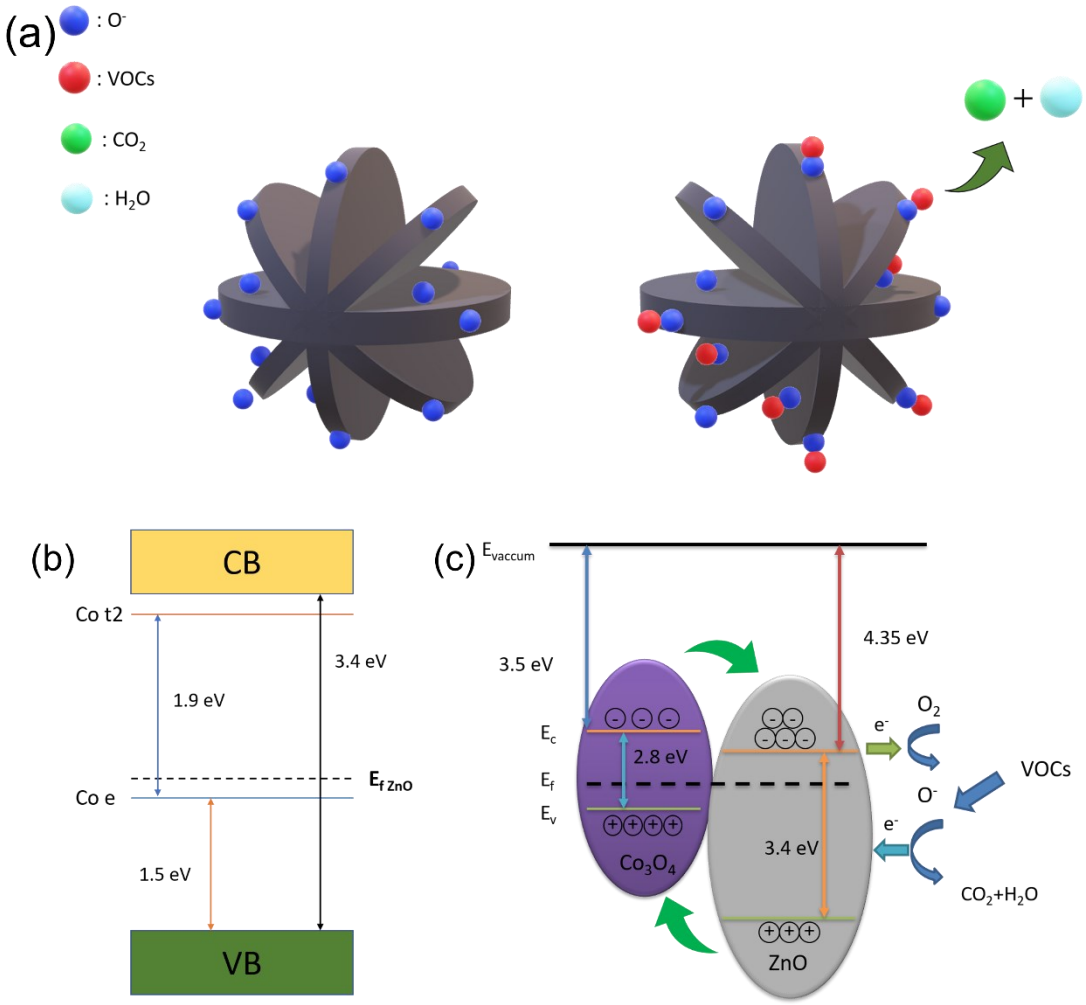

Figure 11. (a) Schematic of the gas sensing process of the Co-ZnO nanoflowers; (b) Band diagram of the Co^{2+} substituted ZnO; (c) Band diagram and electron transfer process during the gas sensing period of the Co_3O_4-ZnO heterojunctions

4. Conclusion

In this work, two kinds of nanosheet-assembled flower of Co-ZnO sensors have been successfully synthesized through the same chemical deposition method by mixing

Co^{2+}, Zn^{2+} and 2-methlyimidazole in water and adding ammonia. The state of Co changed with the amount of Co^{2+} added in the precursor. When Co content is less than 20 at%, Co substituted ZnO can be prepared. When it is higher than 30 at%, Co_3O_4 is generated in the sensing materials. The gas-sensing performance of the Co-ZnO sensors was tested with different kinds of VOCs as biomarkers of lung cancer. The effect of CO_2, relative humidity and VOCs contained in exhaled breath were taken into account as well. The Co substituted ZnO showed good response and long-term stability to isopropanol, while the sensors with Co_3O_4 were more sensitive to acetone. 10Co sensor showed a considerable response to isopropanol with the interference of CO_2 and other VOCs. These results showed the possibility for the usage in e-noses for lung cancer detection. The improvement of the sensing performance can be summarized as the increase of the specific surface area by constructing the porous nanostructure, the doping effect of Co^{2+} and the construction of p-n heterojunctions between Co_3O_4 and ZnO.

Acknowledgment

This work is supported by the Natural Science Foundation of China under Grant No. 51872254, the Outstanding Youth Foundation of Jiangsu Province of China (No. BK20210027), the National Key Research and Development Program of China under Grant No. 2017YFE0115900. The authors would like to thank the European Regional Development Fund (ERDF) and the Walloon Region of Belgium who financially supported this work through the Interreg V France-Wallonie-Vlaanderen program, under PATHACOV project (No. 1.1.297) and the Micro+ project co-funded by the European Regional Development Fund (ERDF) and Wallonia, Belgium (No. 675781-642409). This work was also supported by the Communauté Wallonie-Bruxelles via the WBI-MOST-China (SUB/2019/430254) grant.

References

[1] Bovey, F.; Cros, J.; Tuzson, B.; Seyssel, K.; Schneiter, P.; Emmenegger, L.; Tappy, L., Breath acetone as a marker of energy balance: an exploratory study in healthy humans. Nutrition & Diabetes 2018, 8 (1), 50.

[2 van der Schee, M. P.; Palmay, R.; Cowan, J. O.; Taylor, D. R., Predicting steroid responsiveness in patients with asthma using exhaled breath profiling. Clinical & Experimental Allergy 2013, 43 (11), 1217-1225.

[3] Di Natale, C.; Paolesse, R.; Martinelli, E.; Capuano, R., Solid-state gas sensors for breath analysis: A review. Analytica Chimica Acta 2014, 824, 1-17.
[4] Nardi-Agmon, I.; Abud-Hawa, M.; Liran, O.; Gai-Mor, N.; Ilouze, M.; Onn, A.; Bar, J.; Shlomi, D.; Haick, H.; Peled, N., Exhaled Breath Analysis for Monitoring Response to Treatment in Advanced Lung Cancer. Journal of Thoracic Oncology 2016, 11 (6), 827-837.
[5] Neerincx, A. H.; Vijverberg, S. J. H.; Bos, L. D. J.; Brinkman, P.; van der Schee, M. P.; de Vries, R.; Sterk, P. J.; Maitland-van der Zee, A.-H., Breathomics from exhaled volatile organic compounds in pediatric asthma. Pediatric Pulmonology 2017, 52 (12), 1616-1627.
[6] Rudnicka, J.; Kowalkowski, T.; Buszewski, B., Searching for selected VOCs in human breath samples as potential markers of lung cancer. Lung Cancer 2019, 135, 123-129. [7] Saalberg, Y.; Wolff, M., VOC breath biomarkers in lung cancer. Clinica Chimica Acta 2016, 459, 5-9.
[8] Zhang, C.; Huan, Y.; Li, Y.; Luo, Y.; Debliquy, M., Low concentration isopropanol gas sensing properties of Ag nanoparticles decorated In_2O_3 hollow spheres. Journal of Advanced Ceramics, 2021, accepted.
[9] Song, G.; Qin, T.; Liu, H.; Xu, G.-B.; Pan, Y.-Y.; Xiong, F.-X.; Gu, K.-S.; Sun, G.-P.; Chen, Z.-D., Quantitative breath analysis of volatile organic compounds of lung cancer patients. Lung Cancer 2010, 67 (2), 227-231.
[10] Chen, X.; Xu, F.; Wang, Y.; Pan, Y.; Lu, D.; Wang, P.; Ying, K.; Chen, E.; Zhang, W., A study of the volatile organic compounds exhaled by lung cancer cells in vitro for breath diagnosis. Cancer 2007, 110 (4), 835-844.
[11] Saidi, T.; Moufid, M.; de Jesus Beleño-Saenz, K.; Welearegay, T. G.; El Bari, N.; Lisset Jaimes-Mogollon, A.; Ionescu, R.; Bourkadi, J. E.; Benamor, J.; El Ftouh, M.; Bouchikhi, B., Non-invasive prediction of lung cancer histological types through exhaled breath analysis by UV-irradiated electronic nose and GC/QTOF/MS. Sensors and Actuators B: Chemical 2020, 311, 127932.
[12] Chatterjee, S.; Castro, M.; Feller, J. F., An e-nose made of carbon nanotube based quantum resistive sensors for the detection of eighteen polar/nonpolar VOC biomarkers of lung cancer. Journal of Materials Chemistry B 2013, 1 (36), 4563-4575.
[13] Chen, Q.; Chen, Z.; Liu, D.; He, Z.; Wu, J., Constructing an E-Nose Using Metal-Ion-Induced Assembly of Graphene Oxide for Diagnosis of Lung Cancer via Exhaled Breath. ACS Applied Materials & Interfaces 2020, 12 (15), 17713-17724.
[14] Li, W.; Jia, Z.; Xie, D.; Chen, K.; Cui, J.; Liu, H., Recognizing lung cancer using a homemade e-nose: A comprehensive study. Computers in Biology and Medicine 2020, 120, 103706.
[15] Huan, Y.; Wu, K.; Li, C.; Liao, H.; Debliquy, M.; Zhang, C., Micro-nano structured functional coatings deposited by liquid plasma spraying. Journal of Advanced Ceramics 2020, 9 (5), 517-534.
[16] Li, Y.; Lu, Y.-L.; Wu, K.-D.; Zhang, D.-Z.; Debliquy, M.; Zhang, C., Microwave-assisted hydrothermal synthesis of copper oxide-based gas-sensitive nanostructures. Rare Metals 2021, 40 (6), 1477-1493.
[17] Wu, K.-D.; Xu, J.-Y.; Debliquy, M.; Zhang, C., Synthesis and NH3/TMA sensing properties of $CuFe_2O_4$ hollow microspheres at low working temperature. Rare Metals 2021, 40 (7), 1768-1777.
[18] Zhu, L.; Zeng, W.; Ye, H.; Li, Y., Volatile organic compound sensing based on coral rock-like ZnO. Materials Research Bulletin 2018, 100, 259-264.
[19] Li, W.; Wu, X.; Han, N.; Chen, J.; Qian, X.; Deng, Y.; Tang, W.; Chen, Y., MOF-derived hierarchical hollow ZnO nanocages with enhanced low-concentration VOCs gas-sensing performance. Sensors and Actuators B: Chemical 2016, 225, 158-166.

[20] Meng, F.; Hou, N.; Ge, S.; Sun, B.; Jin, Z.; Shen, W.; Kong, L.; Guo, Z.; Sun, Y.; Wu, H.; Wang, C.; Li, M., Flower-like hierarchical structures consisting of porous single-crystalline ZnO nanosheets and their gas sensing properties to volatile organic compounds (VOCs). Journal of Alloys and Compounds 2015, 626, 124-130.
[21] Dong, X.; Su, Y.; Lu, T.; Zhang, L.; Wu, L.; Lv, Y., MOFs-derived dodecahedra porous Co_3O_4: An efficient cataluminescence sensing material for H_2S. Sensors and Actuators B: Chemical 2018, 258, 349-357.
[22] Hoppe, M.; Ababii, N.; Postica, V.; Lupan, O.; Polonskyi, O.; Schütt, F.; Kaps, S.; Sukhodub, L. F.; Sontea, V.; Strunskus, T.; Faupel, F.; Adelung, R., (CuO-Cu_2O)/ZnO:Al heterojunctions for volatile organic compound detection. Sensors and Actuators B: Chemical 2018, 255, 1362-1375.
[23] Zhou, K.; Ma, W.; Zeng, Z.; Ma, X.; Xu, X.; Guo, Y.; Li, H.; Li, L., Experimental and DFT study on the adsorption of VOCs on activated carbon/metal oxides composites.
Chemical Engineering Journal, 2019, 372, 1122-1133.
[24] Zhang, C.; Huan, Y., Li, Y; Luo, Y; Debliquy, M., Low concentration isopropanol gas sensing properties of Ag nanoparticles decorated In_2O_3 hollow spheres. Journal of advanced ceramics, 2022, accepted.
[25] Miller, D. R.; Akbar, S. A.; Morris, P. A., Nanoscale metal oxide-based heterojunctions for gas sensing: A review. Sensors and Actuators B: Chemical, 2014, 204, 250-272.
[26] Royer, S.; Duprez, D.; Catalytic oxidation of carbon monoxide over transition metal oxides, ChemCatChem, 2011, 3, 24–65.
[27] Luo, Y.; Ly, A.; Lahem, D.; Zhang, C.; Debliquy, M., A novel low-concentration isopropanol gas sensor based on Fe-doped ZnO nanoneedles and its gas sensing mechanism. Journal of Materials Science 2021, 56 (4), 3230-3245.
[28] Geng, X.; Lu, P.; Zhang, C.; Lahem, D.; Olivier, M.-G.; Debliquy, M., Room-temperature NO_2 gas sensors based on rGO@ZnO_{1-x} composites: Experiments and molecular dynamics simulation. Sensors and Actuators B: Chemical 2019, 282, 690-702.
[29] Zhang, C.; Geng, X.; Liao, H.; Li, C.-J.; Debliquy, M., Room-temperature nitrogen-dioxide sensors based on ZnO_{1-x} coatings deposited by solution precursor plasma spray. Sensors and Actuators B: Chemical 2017, 242, 102-111.
[30] Zhang, C.; Geng, X.; Li, J.; Luo, Y.; Lu, P., Role of oxygen vacancy in tuning of optical, electrical and NO_2 sensing properties of ZnO_{1-x} coatings at room temperature. Sensors and Actuators B: Chemical 2017, 248, 886-893.
[31] Zhang, J.; Chen, M.; Zhu, L., Activation of persulfate by Co_3O_4 nanoparticles for orange G degradation. RSC Advances 2016, 6 (1), 758-768.
[32] Rong, F.; Zhao, J.; Su, P.; Yao, Y.; Li, M.; Yang, Q.; Li, C., Zinc–cobalt oxides as efficient water oxidation catalysts: the promotion effect of ZnO. Journal of Materials Chemistry A 2015, 3 (7), 4010-4017.
[33] Zhang, L.; He, W.; Xiang, X.; Li, Y.; Li, F., Roughening of windmill-shaped spinel Co_3O_4 microcrystals grown on a flexible metal substrate by a facile surface treatment to enhance their performance in the oxidation of water. RSC Advances 2014, 4 (82), 43357-43365.
[34] Pillai, P.; Dharaskar, S.; Sasikumar, S.; Khalid, M., Zeolitic imidazolate framework-8 nanoparticle: a promising adsorbent for effective fluoride removal from aqueous solution. Applied Water Science 2019, 9 (7), 150.
[35] Ali, M.; Sharif, S.; Anjum, S.; Imran, M.; Ikram, M.; Naz, M.; Ali, S., Preparation of Co and

Ni doped ZnO nanoparticles served as encouraging nano-catalytic application. Materials Research Express 2020, 6 (12), 1250d5.
[36] Acharyya, D.; Bhattacharyya, P., Alcohol sensing performance of ZnO hexagonal nanotubes at low temperatures: A qualitative understanding. Sensors and Actuators B: Chemical 2016, 228, 373-386.
[37] Cai, X.; Hu, D.; Deng, S.; Han, B.; Wang, Y.; Wu, J.; Wang, Y., Isopropanol sensing properties of coral-like ZnO–CdO composites by flash preparation via self-sustained decomposition of metal–organic complexes. Sensors and Actuators B: Chemical 2014, 198, 402-410.
[38] Wang, S.-C.; Wang, X.-H.; Qiao, G.-Q.; Chen, X.-Y.; Wang, X.-Z.; Wu, N.-N.; Tian, J.; Cui, H.-Z., NiO nanoparticles-decorated ZnO hierarchical structures for isopropanol gas sensing. Rare Metals 2021.
[39] Kortidis, I.; Lushozi, S.; Leshabane, N.; Nkosi, S. S.; Ndwandwe, O. M.; Tshilongo, J.; Ntsasa, N.; Motaung, D. E., Selective detection of propanol vapour at low operating temperature utilizing ZnO nanostructures. Ceramics International 2019, 45 (13), 16417-16423.
[40] Poloju, M.; Jayababu, N.; Manikandan, E.; Ramana Reddy, M. V., Enhancement of the isopropanol gas sensing performance of SnO_2/ZnO core/shell nanocomposites. Journal of Materials Chemistry C 2017, 5 (10), 2662-2668.
[41] Jin, Q.; Wen, W.; Zheng, S.; Wu, J.-M., Enhanced isopropanol sensing of coral-like ZnO–ZrO_2 composites. Nanotechnology 2020, 31 (19), 195502.
[42] Sun, Y.; Wang, Z.; Wang, W.; Li, G.; Li, P.; Lian, K.; Zhang, W.; Zhuiykov, S.; Hu, J.; Chen, L., Electrospinning preparation of Pd@ Co_3O_4-ZnO composite nanofibers and their highly enhanced VOC sensing properties. Materials Research Bulletin 2019, 109, 255-264.
[43] Deng, S.; Liu, X.; Chen, N.; Deng, D.; Xiao, X.; Wang, Y., A highly sensitive VOC gas sensor using p-type mesoporous Co_3O_4 nanosheets prepared by a facile chemical coprecipitation method. Sensors and Actuators B: Chemical 2016, 233, 615-623.
[44] Deng, S.; Chen, N.; Deng, D.; Li, Y.; Xing, X.; Wang, Y., Meso- and macroporous coral-like Co_3O_4 for VOCs gas sensor. Ceramics International 2015, 41 (9, Part A), 11004-11012.
[45] Mansour, E.; Vishinkin, R.; Rihet, S.; Saliba, W.; Fish, F.; Sarfati, P.; Haick, H., Measurement of temperature and relative humidity in exhaled breath. Sensors and Actuators B: Chemical 2020, 304, 127371.
[46] Hahn, S. H.; Bârsan, N.; Weimar, U.; Ejakov, S. G.; Visser, J. H.; Soltis, R. E., CO sensing with SnO_2 thick film sensors: role of oxygen and water vapour. Thin Solid Films 2003, 436 (1), 17-24.
[47] Guo, J.; Li, Y.; Jiang, B.; Gao, H.; Wang, T.; Sun, P.; Liu, F.; Yan, X.; Liang, X.; Gao, Y.; Zhao, J.; Lu, G., Xylene gas sensing properties of hydrothermal synthesized SnO_2- Co_3O_4 microstructure. Sensors and Actuators B: Chemical 2020, 310, 127780.
[48] Yang, M.; Zhang, S.; Qu, F.; Gong, S.; Wang, C.; Qiu, L.; Yang, M.; Cheng, W., High performance acetone sensor based on ZnO nanorods modified by Au nanoparticles. Journal of Alloys and Compounds 2019, 797, 246-252.
[49] Yin, F.; Li, Y.; Yue, W.; Gao, S.; Zhang, C.; Chen, Z., Sn_3O_4/rGO heterostructure as a material for formaldehyde gas sensor with a wide detecting range and low operating temperature. Sensors and Actuators B: Chemical 2020, 312, 127954.
[50] Walsh, A.; Da Silva, J. L. F.; Wei, S.-H., Theoretical Description of Carrier Mediated Magnetism in Cobalt Doped ZnO. Physical Review Letters 2008, 100 (25), 256401.
[51] Li, W.; Wang, G.; Chen, C.; Liao, J.; Li, Z., Enhanced Visible Light Photocatalytic Activity of

ZnO Nanowires Doped with Mn^{2+} and Co^{2+} Ions. Nanomaterials 2017, 7, 20.
[52] Kim, J.-W.; Lee, S. J.; Biswas, P.; Lee, T. I.; Myoung, J.-M., Solution-processed n-ZnO nanorod/p-Co_3O_4 nanoplate heterojunction light-emitting diode. Applied Surface Science 2017, 406, 192-198.
[53] Gao, X.; Li, F.; Wang, R.; Zhang, T., A formaldehyde sensor: Significant role of p-n heterojunction in gas-sensitive core-shell nanofibers. Sensors and Actuators B: Chemical 2018, 258, 1230-1241.